Original Article

MgO-incorporated carbon nanotubes-reinforced Mg-based composites to improve mechanical, corrosion, and biological properties targeting biomedical applications

S. Abazari [a], A. Shamsipur [a,**], H.R. Bakhsheshi-Rad [b,*], M. Keshavarz [c], M. Kehtari [d], S. Ramakrishna [e], F. Berto [f,***]

[a] Department of Materials and Metallurgical Engineering, Amirkabir University of Technology, Tehran, Iran
[b] Advanced Materials Research Center, Department of Materials Engineering, Najafabad Branch, Islamic Azad University, Najafabad, Iran
[c] Department of Materials Science and Engineering, Sharif University of Technology, P.O. Box 11365-9466, Tehran, Iran
[d] Department of Animal Biology, School of Biology, University of Tehran, Tehran, Iran
[e] Department of Mechanical Engineering, National University of Singapore, 9 Engineering Drive 1, Singapore 117576, Singapore
[f] Department of Mechanical and Industrial Engineering, Norwegian University of Science and Technology, 7491 Trondheim, Norway

ARTICLE INFO

ABSTRACT

In this study, magnesium oxide (MgO) nanoparticles are incorporated on carbon nanotubes (CNTs) to reinforce Mg–3Zn–1Mn alloy (ZM31 alloy) by semi-powder metallurgy, followed by hot extrusion, with the purpose of improving the mechanical and biological properties of Mg-based alloy. The microstructural analysis of the nanocomposites indicated a reduction in grain size of Mg alloy with the incorporation of CNTs with a maximum reduction of 61% (ZM31/CNTs), with further reduction in grain size (68%) detected when MgO integrated CNTs composites (ZM31/MgO-CNTs). The compression characteristics of the composites indicate an increase in ultimate compressive strength of 36% and 44%, respectively, with the incorporation of CNTs and MgO-CNTs fillers, and the hardness of Mg alloy increases by 37% and 58%, respectively, with the incorporation of CNTs and MgO-CNTs fillers. The strengthening mechanisms of Mg alloy composites reinforced with MgO-CNTs were discussed. Furthermore, MgO bounded CNTs fillers decelerated the degradation rate of Mg-based alloys, whereas the introduction of CNTs to Mg alloy had a less significant effect. Besides, the ZM31/MgO-CNTs composite indicated superior

---

* Corresponding author.
** Corresponding author.
*** Corresponding author.
E-mail addresses: shamsipur@aut.ac.ir (A. Shamsipur), rezabakhsheshi@pmt.iaun.ac.ir (H.R. Bakhsheshi-Rad), filippo.berto@ntnu.no (F. Berto).

cytocompatibility because of its lower corrosion rates. According to the overall results, the outstanding mechanical performance, appropriate corrosion characteristics, and good cytocompatibility of the ZM31/MgO-CNTs composites verified their potential in medical fields.

1. Introduction

Traditional medical implants, such as titanium alloys and stainless steel, are used in a variety of biomedical applications, particularly in repairing damaged human bone tissue [1—4]. However, the long-term use of such implants raises concerns about toxicity and the ions released [5,6]. Another issue that necessitates the investigation of biodegradable implants is the need for a second surgery to remove the implant behind bone healing [7]. Various biodegradable polymers have recently been employed as temporary medical implants. However, they face issues with inflammation and mechanical strength when used in load-bearing regions [8—10]. Mg alloys show prospective use as degradable solid tissue implant materials owing to their high biocompatibility and mechanical characteristics compared to other biodegradable implant materials already being employed [11,12]. However, Mg alloys do not exhibit the unfavorable influence of stress shielding, which is common in traditional metallic implants made of stainless steel or titanium alloy that are frequently utilized for bone regeneration [13—15]. Besides, Mg degradation products are not really detrimental to the human body and may potentially promote human bone growth and regeneration [16]. On the other hand, Mg alloys are prone to significant corrosion rates and H_2 gas evolution in body fluid, leading to implant failure before the complete healing process [10,17—19]. Because of such limitations, monolithic Mg has not been utilized directly in-service circumstances. Incorporating reinforcement phases and alloying elements are required to mitigate these limitations and improve Mg characteristics. The most commonly used techniques for achieving higher properties in Mg are alloying and composite processing. Non-toxic alloying elements are required for bio-Mg alloys; hence zinc (Zn), calcium (Ca), and manganese (Mn) have been proposed as alloying elements for medical purposes [20]. In this regard, Yin et al. [21] showed that the yield strength, elongation, and tensile strength of as-cast Mg−Zn−Mn alloys improved with boosting Zn content, with 3.0 wt. % Zn provides the highest mechanical property. The corrosion resistance property of the as-cast Mg−Zn−Mn alloys appeared to decrease as the concentration of Zn was escalated to 3.0 wt.%. Also, Xu et al. [22] have developed Mg−Mn−Zn alloys with excellent corrosion resistance and mechanical characteristics [15].

Carbon nanotubes (CNTs) are a unique material because of their interesting mechanical and electrical characteristics. Because of their adaptability, they are employed in a wide range of uses. CNTs are used in a variety of sectors, including gas sensors or biosensors [23], electronics [24], biomaterial correction, and additives for ceramics, polymers, or metal composites [25]. The unique properties of carbon nanotubes, such as their great tensile strength and Young's modulus, offer them an excellent option for developing composite containing CNTs, polymeric and ceramic coatings. Incorporating CNTs into these matrices enhances mechanical characteristics, particularly in uses requiring great mechanical strength or are subjected to severe situations [26].

Furthermore, the CNT has a high aspect ratio, suggesting a great surface area to volume ratio (SA/V) [27]. CNT has been employed with various materials in attempts to develop useful composite materials due to its unique characteristics and great SA/V ratio [28—30]. As a result, CNTs reinforced Mg matrix composites are experimentally manufactured and demonstrate significant mechanical characteristics, effective in meeting the critical requirements of high-strength and light-weight metal materials [31]. Sun et al. [32] developed an in-situ method for growing CNTs on the surface of Mg powders in order to acquire distributed CNTs evenly in the composite. Nevertheless, because of the weak contact bonding between CNTs and matrix, the ductility of the composite is relatively low (only 1.9% fracture strain attained). Rashad et al. [33] used powder metallurgy to create CNTs reinforced Mg−3Al−1Zn composites with a high fracture strain (17.9%). Similarly, Endo et al. [34] found that AZ91D containing CNTs (AZ91D/CNT composite) had better corrosion resistance than pristine AZ91D. According to their findings, CNTs work as a water repellent and enhance the surface protective coatings. However, few attempts have been made so far to prepare ZM31/MgO-CNTs composites with high mechanical performance and suitable corrosion behavior. In this investigation, Mg−Zn−Mn matrix composites strengthened with MgO incorporated CNTs via semi-powder metallurgy, accompanied by hot extrusion. The influences of MgO incorporated CNTs on the microstructure, corrosion behavior, and the mechanical characteristics of the Mg−Zn−Mn alloy matrix were studied.

2. Materials and methods

2.1. Materials preparation and microstructural characterization

The ZM31/MgO-CNTs composites were fabricated via the semi-powder metallurgy process (as shown in Fig. 1). Proper contents of Mg (99.8% purity, 50 μm mean particle size), Zn powder (98.8% purity, 7.5 μm mean particle size) and Mn (99.5% purity, 45 μm average particle size) powders were the first ball-milled in Ar atmosphere (3 ppm oxygen) in a
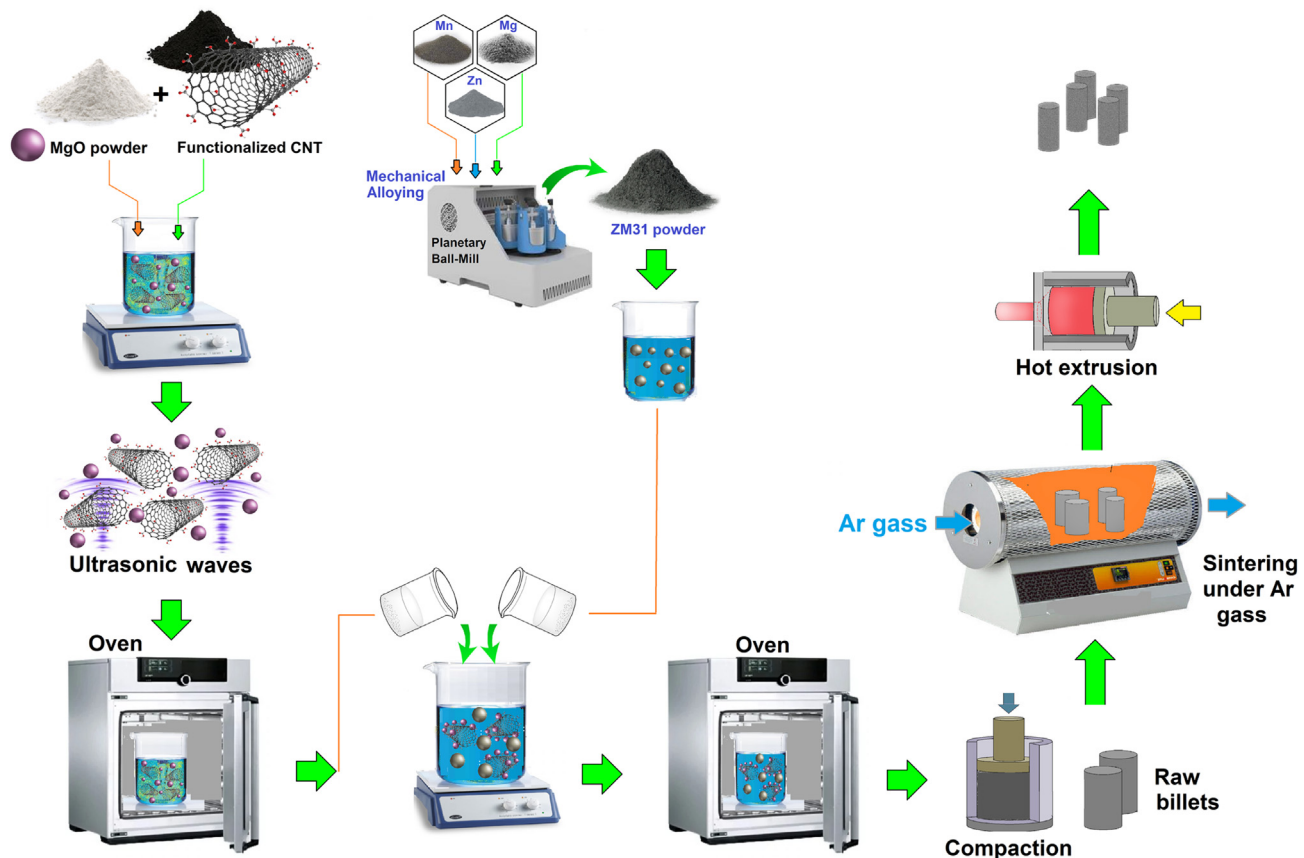
Fig. 1 — Schematic of the preparation of MgO-CNTs/ZM31 composite via semi-powder metallurgy synthesis.

planetary ball mill with a 20:1 ball to powder ratio and a speed of rotation of 300 rpm for 25 h in argon atmosphere (<3 ppm oxygen) with Mg—3Zn—1Mn alloy to prepare the ZM31 alloy. The MgO-coated CNTs were prepared using a hydrothermal method based on Ref. [35]. MgO-coated CNTs were independently dispersed in ethanol by ultra-sonication for 2 h to prepare ZM31/MgO-CNTs composites. It's worth noting that the formation of disordered atoms by diffusion between MgO and CNTs at the interface during the manufacturing process results in strong interfacial bonding between MgO and CNTs [36]. Suspensions of CNTs, MgO, and Mg alloy were then stirred together and mechanically agitated for 1 h to create ZM31/MgO-CNTs composite suspensions, which were then filtered and vacuum-dried at 313 K for 12 h to produce ZM31/MgO-CNTs composite mixture [36]. The as-prepared composite mixtures were pressed in a 40 mm wide and 200 mm height cylinder mold at a hydraulic pressure of 120 MPa. The compacts then were sintered for 2 h in an Ar atmosphere tube furnace at 873 K. The homogeneous compacts were hot extruded at 673 K with an extrusion ratio of 11:1. In this respect, the Mg alloy and the counterpart ZM31/CNTs and ZM31/MgO-CNTs composites were fabricated using the same techniques (compacting, sintering, and extrusion).

The microstructure of specimens was studied using optical microscopy (OM) and scanning electron microscopy (SEM; JEOL JSM-6380LA) with an energy dispersive spectrometer (EDS). Mechanically ground, polished, and etched specimens for OM and SEM investigations in a solution of 75 vol. % ethylene glycol, 25 vol. % H_2O and 1 vol. % HNO_3 [37]. After the immersion tests, an X-ray diffractometer (Siemens-D500) was used to detect the phases that comprise the materials using Cu-Kα radiation and the corrosion products developed on the specimen's surface. To determine the structural changes of CNTs in nanocomposites, a Raman spectrometer (Takram P50C0R10 with a laser wavelength of 532 nm) was used.

2.2. Mechanical test

The Vickers hardness values of the materials were determined using a micro-Vickers hardness tester (Shimadzu) with a 100 g applied load for 10 s. In the case of samples, the hardness was measured in the grain interiors. Uniaxial compression testing was performed at room temperature on an Instron 3365 testing equipment at a steady nominal strain rate of $7 \times 10^{-4} s^{-1}$. The test specimens, which were $3 \times 6 mm^2$ in size, were fabricated in accordance with ASTM-E9-09 [38]. For the compressive tests, five identical samples were used.

2.3. In-vitro corrosion test

Potentiodynamic polarization experiments were performed with the PARSTAT 2263 potentiostat/galvanostat (Princeton Applied Research) at $37 \pm 1\,^{\circ}C$ in SBF solution. The specimens were ground using SiC sandpaper (up to 2000 grit) before

being polished with diamond paste. The specimens were cleaned in ethanol ultrasonically after polishing. The clean specimens were molded in Teflon with a 1 cm^2 exposed surface and then immersed in the SBF solution. An electrochemical cell was equipped with a graphite counter electrode, a specimen as a working electrode and a saturated calomel electrode (SCE) as a reference electrode. Specimens were immersed in the solution until a consistent open circuit potential (OCP) was achieved. Following the 1 h immersion, polarization experiments were performed in the potential range of ±250 mV$_{SCE}$ at a scan rate of 1 mV/s, starting at 250 mV below the OCP. The electrochemical impedance spectra (EIS) were evaluated in a frequency range of 10^5 to 10^{-2} Hz and analyzed with the ZsimpWin software. The Metrohm Auto-lab PGSTAT30 machine was also used for the EIS test. Each electrochemical experiment was repeated to ensure that the results were reproducible. The immersion test was performed in accordance with ASTM G31-72 [39]. The samples were then immersed in a beaker containing 200 ml of simulated body fluid (Kokubo fluid). During the testing time, the SBF was not replenished. After that, the specimens were washed with acetone and deionized water in order to completely remove any corrosion products before being weighed. The corrosion rate was determined in the following manner:

$$C_R = \frac{W}{Atd} \quad (1)$$

where C$_R$ is the corrosion rate (also referred to as the average corrosion rate, C$_R$), A is the surface area subjected to the corrosive fluid, W is the mass loss, t is the immersion time and d is the density. During the soaking experiment, the mean pH value of the SBF from three observations was recorded every 12 h. Inductively coupled plasma atomic emission spectroscopy (ICP-AES) was utilized to determine Mg ion concentrations in immersion solutions, with a blank SBF solution as a control. After 7 days of immersion, each sample was removed from the solution.

2.4. In-vitro biocompatibility test

In vitro cell experiments were utilized to assess biocompatibility for cytotoxicity. The medium extraction was a MEM serum-free solution, and the extracts were obtained with a surface area to medium extraction ratio of 0.7 cm^2/ml in humidified air at 37 °C and 5 vol.% CO$_2$ for 1 and 3 days, respectively. Prior to the cytotoxicity test, the extracts were gathered, centrifuged and filtered before being stored at 4 °C. MG-63 cells were cultured in Dulbecco's Modified Eagle's Medium (DMEM), 10% fetal bovine serum (FBS), 100 U/ml penicillin, and 100 mg/ml streptomycin at 37 °C in a humidified atmosphere of 5% CO$_2$. In vitro cytotoxicity experiments were performed using indirect contact, as recommended according to ISO 10993-5. Negative and positive controls were MEM medium and MEM medium with 0.64% phenol, respectively. Cells were incubated for 12 h in 96-well cell culture plates to induce adhesion, with 5 × 10^3 cells/100 ml medium in each well. All wells were aspirated, and 100 ml of extracts were added, resulting in three replicates for each sample. Following that, all wells were incubated for 24 h in accordance with

Ref. [40]. Besides, alkaline phosphatase (ALP) staining was used to assess MG-63 cell differentiation potential in extracts after 1 and 3 days of culture. The cultured cells were washed 3 times with PBS before being fixed in 4% paraformaldehyde for 30 min. The fixed cells were stained with Biyuntian's ALP staining kit after rinsing 3 times with PBS as described in Ref. [41].

2.5. Statistical analysis

The obtained measurements from independent tests were averaged and analyzed with SPSS 19.0 software. Student's t-tests were used to compute p values between groups, and the variation was assessed significantly when *p < 0.05 and **p < 0.01.

3. Results and discussion

3.1. Microstructure evaluation

The morphology of the samples and the effect of CNTs and ZM31/MgO-CNTs were studied by FE-SEM and TEM. In the as-received condition, the CNTs are severely tangled together, as shown in Fig. 2a; this type of morphology would reduce the effectiveness of CNTs as reinforcement. The TEM image of the CNTs after the dispersion technique utilized in this investigation is shown in Fig. 2b. In comparison to the pre-dispersion step, CNTs aggregates were almost absent, and individual CNTs were discovered to have diameters in the 8 nm range. Furthermore, as shown in Fig. 4d, the MgO-CNTs reinforcement is well dispersed in the Mg alloy matrix. When MgO was added to CNTs suspensions during the semi-powder metallurgy process, MgO bound onto the CNTs surface, as shown in Fig. 2d. The surface of the CNTs was uniformly covered with MgO, implying a homogeneous grafting of MgO surrounding CNTs. The incorporation of MgO onto the surfaces of the CNTs was evaluated using TEM images of the ZM31/MgO-CNTs, which are shown in Fig. 1d-f. As a result, it was indicated that CNTs with a diameter of ~8 nm were intertwined with MgO in a spherical shape in the Mg alloy matrix [42]. MgO-CNT aggregates were almost observable in the matrix of Mg-based particles. CNTs were coated with MgO, leading to the surface of the carbon other than sp^2 and the MgO was tightly connected to the CNTs because of robust electron interactions between the hydroxyl groups MgO in the matrix of Mg-based particles. As a result, it was demonstrated that CNTs with a diameter of ~8 nm were intertwined with MgO in a spherical shape in the matrix Mg alloy [43].

Optical microscopy was also used to study the grain structure of Mg alloy, ZM31/CNTs, and ZM31/MgO-CNTs composites. It can be seen that the CNTs/Mg composite was made up of the Mg matrix, and the grain size progressively reduced as more CNTs were added. The addition of MgO to the ZM31/CNTs combination reduced the grain size even further. The linear intercept method was used to determine the average grain size of ZM31/MgO-CNTs composites. Furthermore, it was clearly demonstrated that the grain size rapidly decreased from 23.4 μm for ZM31 alloy to 9.1 μm for ZM31/CNTs composite and gradually reduced to 7.3 μm for ZM31/
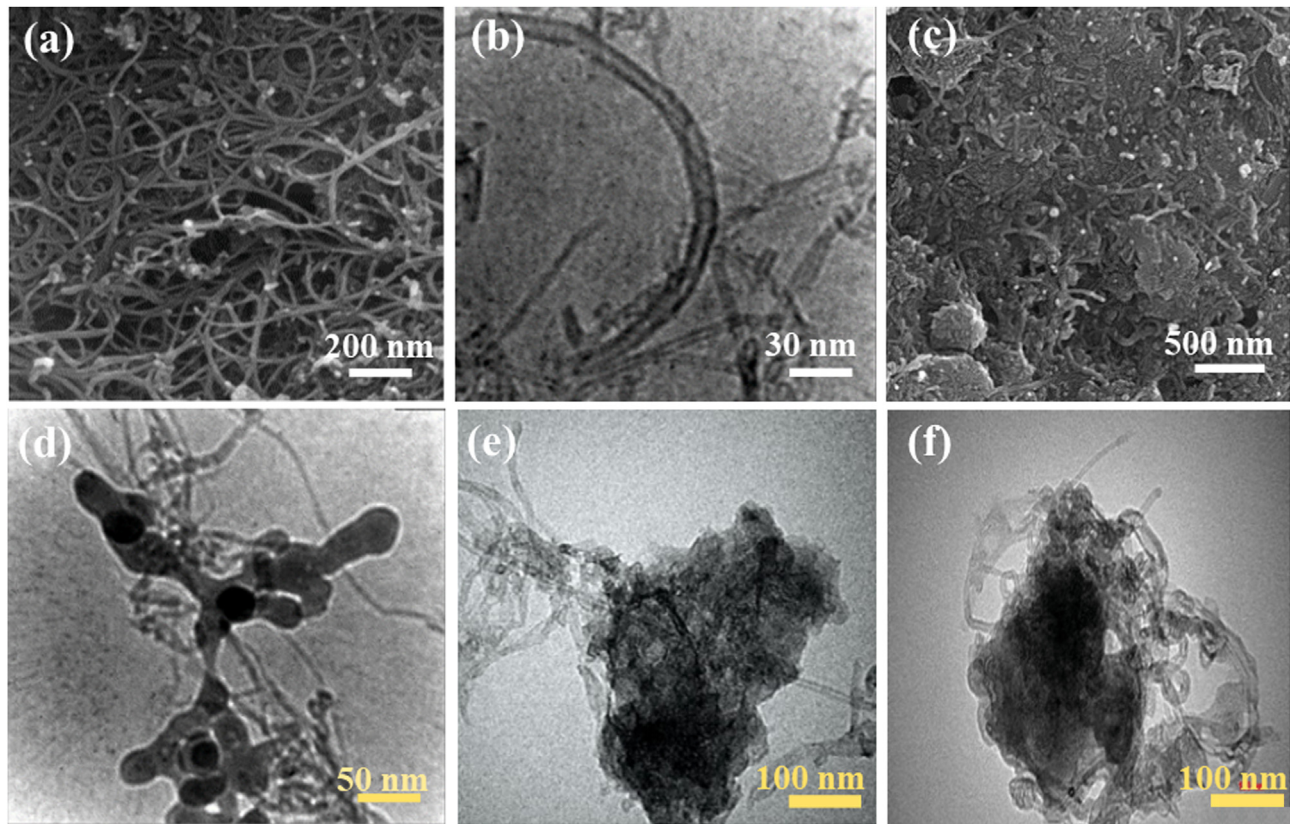
Fig. 2 — FE-SEM and TEM micrographs of (a, b) CNTs, SEM micrograph of (c) ZM31/MgO-CNTs composite powder, TEM images of (d) MgO-CNTs powder and (e,f) ZM31/MgO-CNTs composite powders.
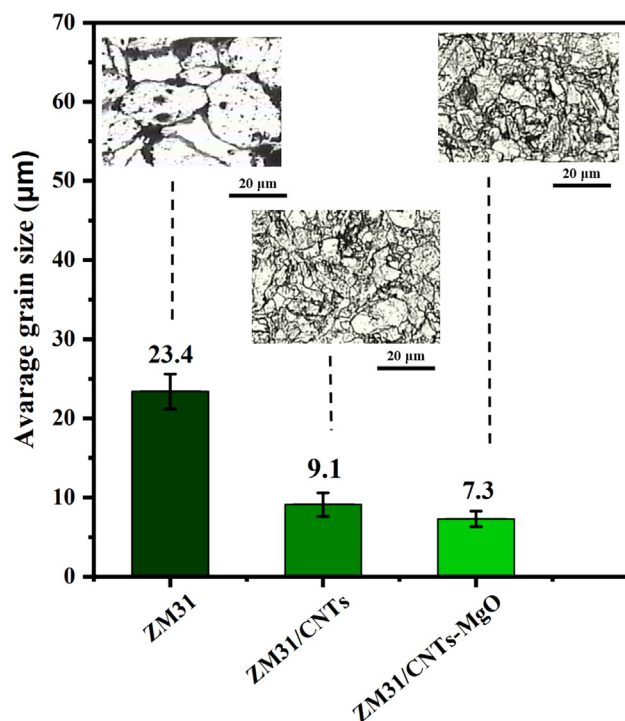

Fig. 3 — OM image and grain size calculations of ZM31 alloy matrix, CNTs/Mg, and CNTs-MgO/Mg composites.

MgO-CNTs composite (Fig. 3), demonstrating the grain refinement influence of MgO and CNTs on Mg matrix.

The elemental mappings of the ZM31/MgO-CNTs composite are shown in Fig. 4a-d depicts the elemental mappings of the ZM31/MgO-CNTs composite. It implies that the C and O elements were distributed evenly, implying that the CNTs and MgO nanofillers in theZM31/MgO-CNTs composite were distributed uniformly. The presence of C and O, in addition to Mg, Zn, and Mn, was confirmed by EDS analysis of the ZM31/MgO-CNTs composite, which is related to the Mg alloys matrix (Fig. 4e). This further confirms that CNTs bond well with MgO and Mg matrix. It should be noted that the graphitic sheets were very evident. However, one of the major challenges in the synthesis of ZM31/CNTs nanocomposites is the insufficient interfacial bonding between CNTs and the matrix of Mg alloy [44]. It is worth noting that the MgO nano-reinforcements are semi-coherent with the surrounding Mg matrix in the composites, indicating a significant interfacial bonding. Because MgO has a really small interatomic spacing misfit (4.7%) along with the matching directions, this interfacial structure characteristic is also useful in the grain refinement of Mg matrix composite. The impingement of the interface reaction between the Mg matrix and the residual oxygen in GNS has been suggested to be another reason for the high density of dislocations near the interface [45]. The presence of dislocations facilitated the strengthening of this bonding interface [46,47]. The schematic in Fig. 4f shows the CNTs/MgO interface with the characteristics of nanoscale-
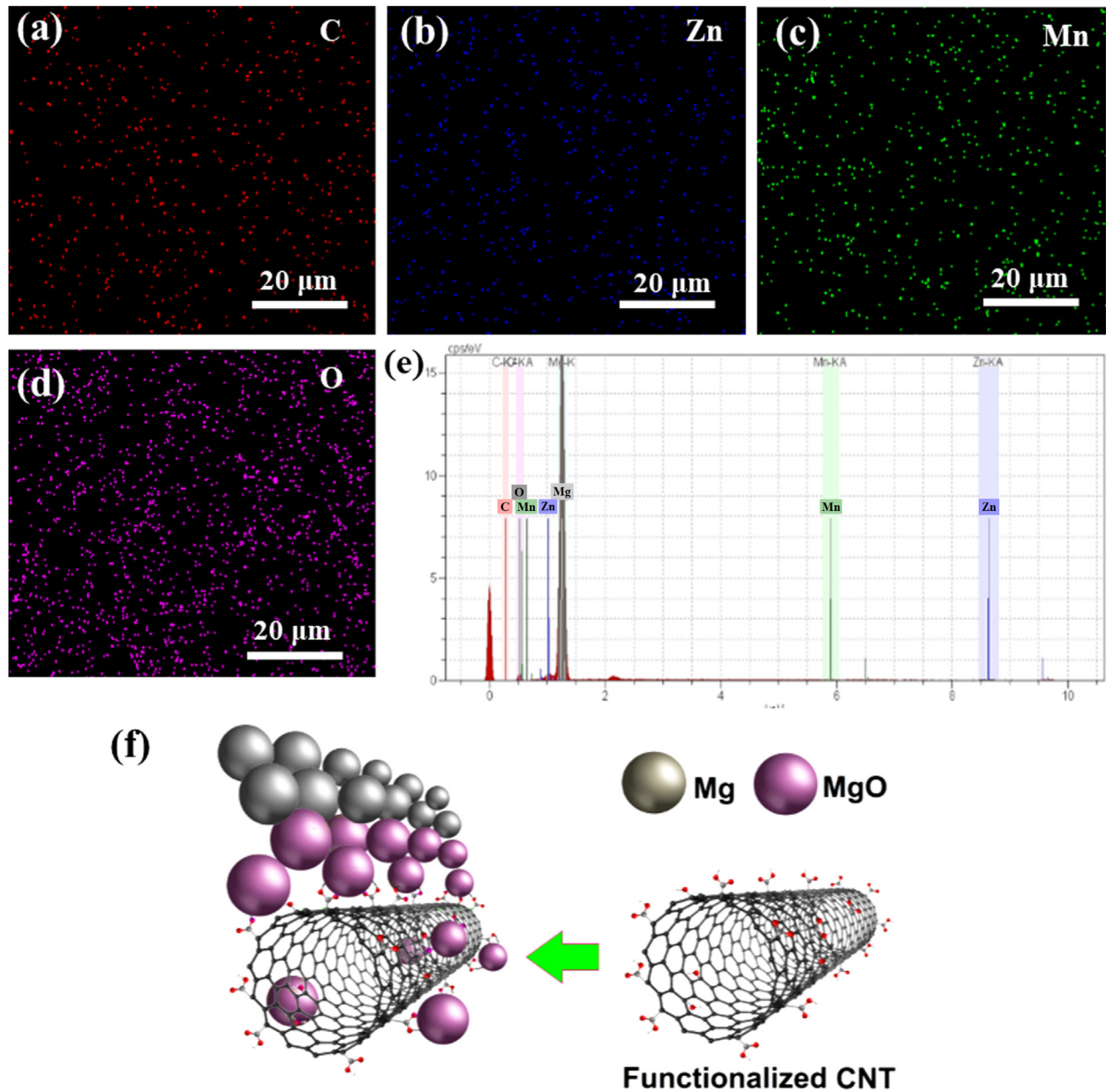
Fig. 4 – Elemental map of ZM31/CNTs-MgO composite showing elemental mapping: (a) C element, (b) Zn element, (c) Mn element, (d) O element, (e) EDS analysis, and (f) Schematic illustrations bonding between MgO-CNTs and Mg alloy matrix.

contact and diffused interfacial bonding, showing the formation of a strong interfacial bonding in the composite; On the other hand, the diffused interfacial bonding between reinforcement and the matrix was also confirmed to be a kind of strong interfacial bonding.

Yuan et al. [36] have reported that two types of bonds were formed at the CNTs/MgO interface: nanoscale-contact bonds and diffused interfacial bonds. However, when the surface of Mg interacts with MgO-incorporated carbon nanotubes, more MgO nanoparticles are attached to the CNT surface, as shown in this study. The nucleation of oxide islands on the surface of Mg particles will then proceed until the island saturation concentration is reached. In this case, the existence of MgO

nanoparticles not only creates a powerful interfacial interaction between the CNT reinforcement and the Mg matrix, but it can also impede dislocation motion by producing a dislocation loop, resulting in composites with increased strength. Correspondingly, the evaluated interfacial distance between MgO and CNT surface ($d_{CNT-MgO}$) was reported to be 0.3650 nm, implying nanoscale-contact interfacial bonding [36]. Their findings also revealed a diffused bonding interface was created in the composite between CNTs and MgO. Furthermore, based on the d-spacing values of Mg and CNTs, the (0002) plane of CNTs crossed the (2110) α-Mg and (1011) α-Mg planes with angles of 98° and 50°, respectively. This demonstrates that CNTs are principally incoherent with the α -Mg
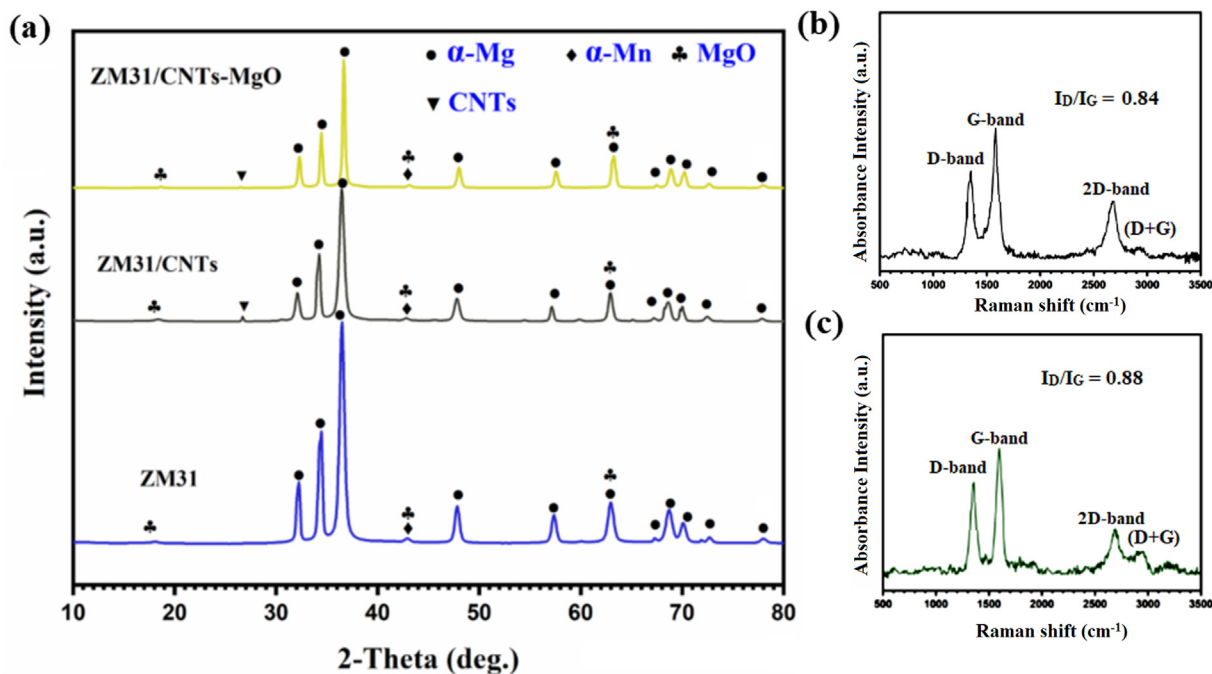
Fig. 5 – XRD patterns of ZM31 matrix alloy, ZM31/CNTs and ZM31/CNTs-MgOcomposites; and Raman spectra of (b) raw CNTs and (c) MgO-CNTs/Mg composites.

matrix in the composite. Simultaneously, the carbon atoms of CNT were tightly integrated with Mg atoms at a specific angle, resulting in lattice distortion of the Mg matrix due to a mismatch in the coefficients of thermal expansion (CTE) of CNT (2.7×10^{-6} K^{-1}) and Mg (25×10^{-6} K^{-1}) [47]. Due to the difference in atomic layer space of wall space of CNT (0.37 nm) and Mg (0.26 nm), it is easier to develop a good grip in the mismatch area, and the integrated structure and/or sandwich structure formed between Mg matrix and CNT induces firmly bonding interaction between Mg matrix and CNT [3].

Fig. 5a depicts the results of X-ray diffraction characterization of as-received Mg alloy, ZM31/CNTs, and ZM31/MgO-CNTs composite powders. Peaks corresponding to CNTs can be found at 2θ equal to 26.54°. In the case of Mg alloy, α-Mg and a small amount of α-Mn phase were the only peaks observed. Due to the limited mass content of CNTs, the XRD spectrum of ZM31/CNTs composites did not indicate any peaks other than the Mg-based matrix [48]. The presence of MgO bound to the surface of CNTs (ZM31/MgO-CNTs composite) results in the appearance of additional peaks for the composite powder mixtures. Furthermore, some MgO diffraction peaks at 2θ equal to 42.9° and 62.86° (JCPDS Card 86–0441) can only be seen in the profile indicative of crystalline MgO formation [49]. The intensity of the CNTs and MgO peaks is very low, with only a few peaks appearing in the composite powder mixtures, which could be due to the low weight fraction of reinforcements in the Mg alloy matrix. Only peaks corresponding to α-Mg and MgZn phases were observed in the case of ZM31/MgO-CNTs, indicating the absence of any inter-metallic formation between Mg alloy and reinforcements (MgO-CNT) [47].

To evaluate the structural changes of CNTs during the fabrication process, Raman spectra were recorded for the ZM31/MgO-CNTs composite (Fig. 5b,c). The Raman spectra of CNT powders clearly show a D-peak at 1317 cm^{-1} related to disorder structural defect because of sp^3 carbon bonds, a G-peak at 1566 cm^{-1} related to stretching bond of sp^2 carbon atoms in the graphitic lattice, and a 2D-peak at 2684 cm^{-1} attributed to sensitive to the number of graphitic atomic layers [50]. The I_D/I_G value increased only slightly after fabrication, from 0.84 to 0.88, indicating that most of the CNTs were not damaged during the dispersion and hot extrusion processes, and only minor disordering and structural defects occurred in this material. The integrity of carbon nanotubes (CNTs) is critical to their strengthening effect.

3.2. Mechanical properties

Micro-hardness measured on the cross-sections of the Mg alloy, ZM31/CNTs, and ZM31/MgO-CNTs composites can be seen in Fig. 6a. As shown in the results, the mean micro-hardness of the Mg alloy increases monotonically with the addition of CNTs. The micro-hardness of Mg alloy is 51.6 HV, whereas ZM31/CNTs and ZM31/MgO-CNTs composites have values of 74.5 and 83.4 HV, respectively. Compressive strength experiments were used to evaluate the influences of MgO-CNTs on mechanical characteristics of ZM31/MgO-CNTs composites (Fig. 6b). After the addition of CNTs to Mg alloy, the compressive strength increased from 295.6 ± 20.4 MPa to 404.8 ± 16.1 MPa. Meanwhile, the compressive strength of the ZM31/MgO-CNTs composite gradually increased to a peak of 429 ± 15 MPa. The preservation and distribution of CNTs in the composite are critical for reinforcing the weak mechanical characteristics of Mg alloy [51,52]. CNTs in the composite created an extremely well-distributed web in this study, and
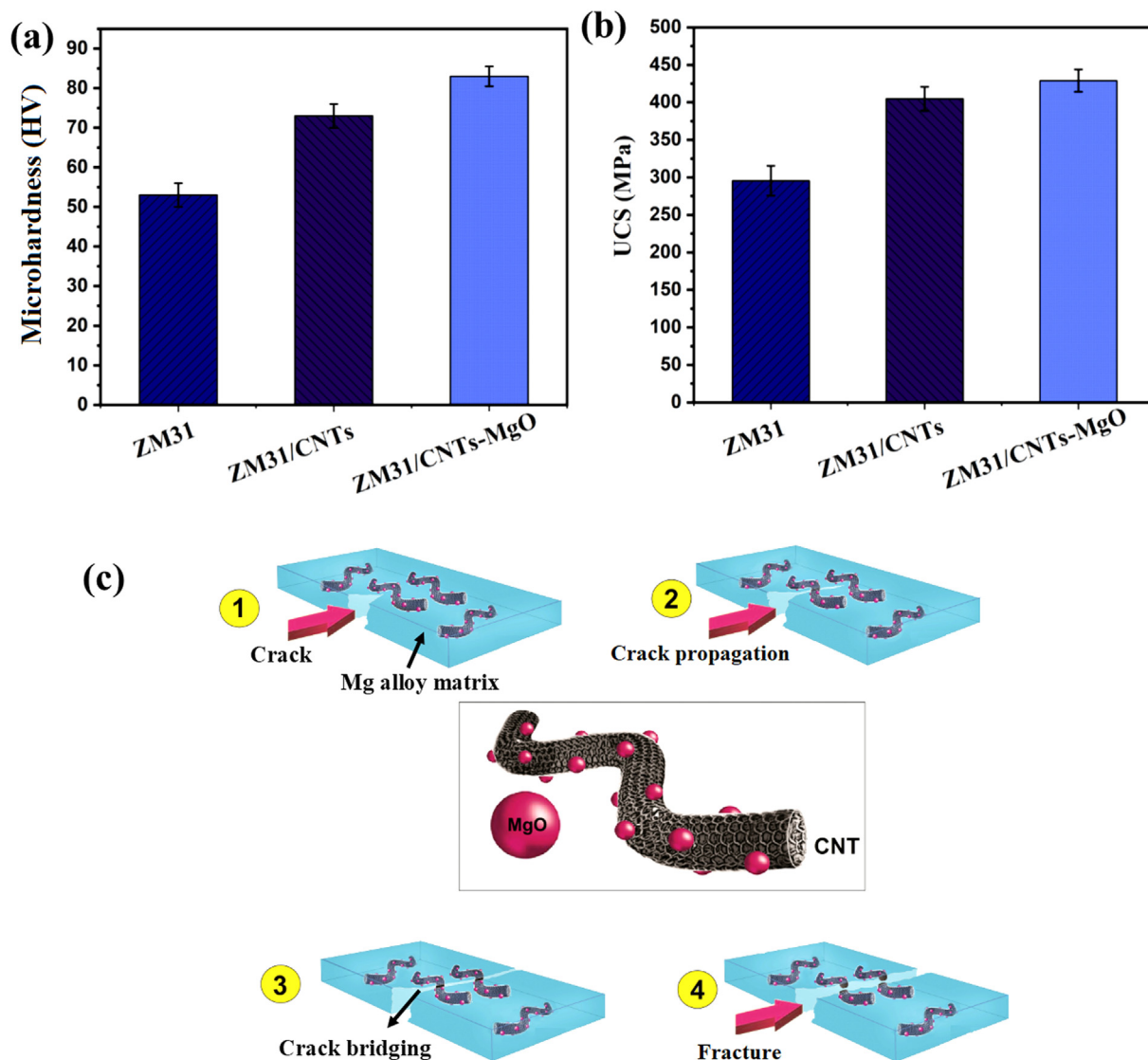
Fig. 6 – (a) Microhardness, (b) compressive curves of ZM31 alloy, ZM31/CNTs and ZM31/MgO-CNTs composites and (c) schematic of reinforcing mechanisms of MgO-CNTs in Mg-based alloy.

some MgO-CNTs were anchored to Mg particles to fabricate bridge structures (Fig. 6c). The fracture toughness and bonding strength of Mg alloy were improved by the evenly distributed MgO-CNTs [53]. In this regard, another study found that as the CNTs content in the powder mixture boosted, the microhardness and bonding strength of the ZM31/CNTs composite coating increased, indicating the brittle nature of Mg alloy might be greatly affected by the incorporation of MgO-CNTs [51]. It is worth noting that when MgO-incorporated CNT reinforcement is added to Mg alloy, grain size refinement occurs, resulting in an enhancement in the fraction of grain boundary. Grain boundaries act as a barrier to dislocation motion, one of the main factors of strengthening [54]. Furthermore, the uneven incorporation of MgO-CNT particles into the Mg alloy matrix can function as barriers, obstructing dislocation motion. One of the essential aspects of grain refinement is that it improves toughness simultaneously as it improves strength [55].

The evident improvement in mechanical characteristics of ZM31/MgO-CNTs composites is due to the effective load transfer at the ZM31/MgO-CNTs interface and the reinforcement roles of MgO incorporated CNTs filler to the Mg alloy matrix. The formation of a strong chemical bond with MgO incorporated CNTs and the preservation of the exceptional structure of CNT. This results in high interfacial bonding strength and efficient load transfer capacity at the ZM31/MgO-CNTs interface. During the fracture process, a load can be effectively transferred from the Mg alloy matrix to the MgO-attached CNT reinforcer. As a result, more fracture energy is consumed by the pulled-out and bridged CNTs, resulting in improved mechanical properties. Furthermore, in ZM31/MgO-CNTs composites, changing the orientation of crack propagation to some extent improves fracture toughness [56]. It has been reported that the increased elongation and strength in ZM31/CNTs nanocomposite compared to ZM3 alloy is mostly due to different aspects: (a) the efficient and strong interface
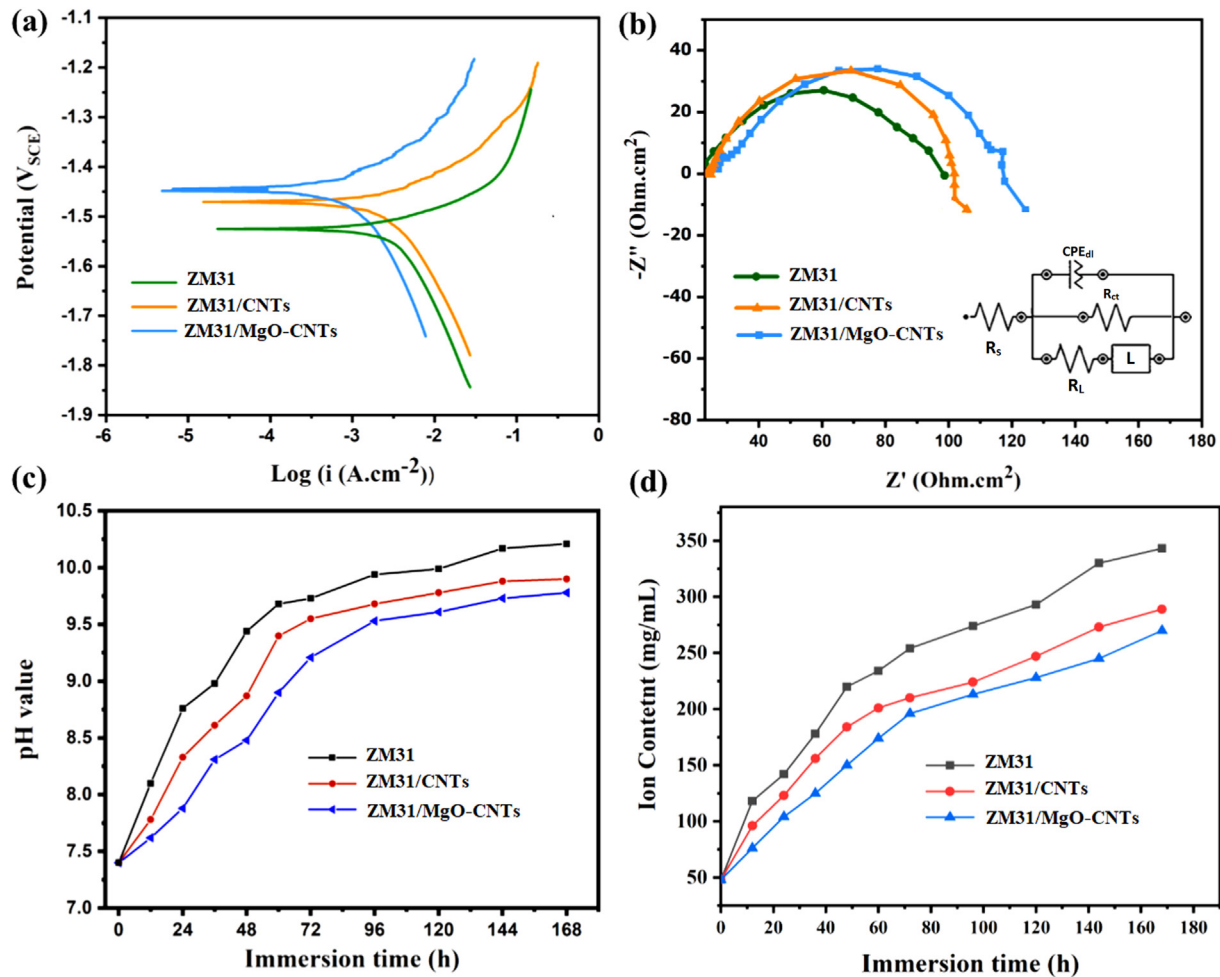
Fig. 7 — (a) Potentiodynamic polarization curves and (b) Nyquist plots and equivalent circuit used to model the results of composites, and (c) variation of pH value and (d) Mg ion concentrations released from ZM31 alloys, ZM31/CNTs and ZM31/MgO-CNTs nanocomposites after different immersion time in the SBF.

bonding among CNTs and Mg alloy matrix and (b) the nano-sized second phase particle [42]. Similarly, it has been reported that the mechanical characteristics of the composite are highly connected to the dispersion and interface strength of CNTs inside the matrix [57]. CNTs have the capacity to bear external stress and prevent crack development via bridging and pull-out mechanisms and also CNT-induced fracture mode transition [58]. Because the EDX-mapping images prove good uniformity of the Mg-based composite structure, we interpret the enhanced mechanical characteristics as an even more homogenous distribution of MgO-attached CNTs reinforcer across the Mg alloy-based matrix. Furthermore, one may assume that it is possible that the orientation of MgO-

attached CNTs in the nanocomposite with respect to the substrate influences the overall final performance and characteristics of the ZM31/MgO-CNTs composite. For example, according to the results of this current study, it has been discovered that a non-covalently functionalized CNT aligned with the matrix that responds to load transfer and could be a possible assumption for improved mechanical characteristics [55].

3.3. Electrochemical measurements

Potentiodynamic polarization is utilized to assess the corrosion resistance of the composites, with the Mg alloy curve acting as a reference. Fig. 7a depicts the potential E in V vs. an SCE electrode as a function of current density i_{corr} for the Mg alloy, ZM31/CNTs, and ZM31/MgO-CNTs composites. Table 1 also quantitatively summarizes the corrosion experiment data in terms of corrosion current density (i_{corr}) and corrosion potential (E_{corr}), which are determined using anodic branch extrapolation. The Mg alloy and ZM31/CNTs composite have lower E_{corr} of -1.53 V_{SCE}, and -1.47 V_{SCE}, respectively, as well as higher i_{corr} values of around 121.34 and 101.56 $\mu A/cm^2$,

Table 1 — Electrochemical parameters obtained from potentiodynamic polarization curves.

Samples	E_{corr} (V_{SCE})	i_{corr} ($\mu A/cm^2$)	C_R (mm/year)
ZM31 alloy	−1.53	121.34	2.77
ZM31/CNTs	−1.47	101.56	2.32
ZM31/MgO-CNTs	−1.43	86.73	1.98

indicating the addition of CNTs into Mg-based composites, improves corrosion resistance. MgO bound CNT reinforcer could improve the performance of Mg-based composites by causing further changes to the positive direction of E_{corr} (−1.43 V_{SCE}) and more reduction of i_{corr} values (86.73 μA/cm^2) was observed compared to the Mg alloy [59]. The Nyquist diagram (Fig. 7b) indicates that the records form a common semicircle (capacitive loop) with various radii; also, it demonstrates that the charge transfer resistance (R_{ct}) of the ZM31/MgO-CNTs composite is around 131.61 Ω cm^2, that is more than that of the Mg alloy (96.48 Ω cm^2). To characterize the samples, the electrochemical impedance spectroscopy (EIS) spectra in a simple equivalent circuit would be used where Rs denotes the solution resistance, CPE-film is the corrosion product capacitance, R_{ct} is the charge transfer resistance and CPE-dl is the electric double-layer capacitance of the passive film. The R_{ct} value of ZM31/MgO-CNTs composite is greater than that of Mg alloy and ZM31/CNTs, implying that the formation of a uniform corrosion product film over the composite enhances corrosion barrier function. The Mg alloy indicates the lowest R_{ct}, causing the formation of a porous and loose protective film like that of Mg(OH)$_2$, which cannot adequately guard the substrate against corrosive medium penetration [60,61]. The reduction in the number of pores and voids in the ZM31/MgO-CNTs composite (Fig. 7b) induced by the MgO-bound CNT surface reinforced the alloy matrix could be related to the visibly larger R_{ct}. The existence of smaller pores and voids in the matrix of the composite resulted in reduced corrosive solution penetration into the ZM31/MgO-CNTs composite matrix, which can efficiently decrease its area of contact with the corrosive solution, thereby enhancing R_{ct}.

Fig. 7c and 7d depicts the change in pH and Mg^{2+} ions concentration in the SBF as time-dependent throughout immersion of all studied specimens. Recent investigations have indicated that the fluctuation in pH and the concentration of Mg^{2+} ions correspond with the corrosion resistance of Mg alloy [62]. During the initial stage of immersion, all specimens experienced a quick boost in the pH and the concentration of Mg^{2+} ions of the SBF medium due to the rapid Mg-based degradation based on reactions (2−4):

$$Mg \rightarrow Mg^{2+} + 2e^- \qquad (2)$$

$$2H_2O + 2e^- \rightarrow H_2 + 2OH^- \qquad (3)$$

$$Mg^{2+} + 2OH^- \rightarrow Mg(OH)_2 \qquad (4)$$

The rate of great pH and Mg^{2+} ions concentration of the SBF solution was delayed gradually as the immersion time increased. This may be due to the creation of a protective Mg(OH)$_2$ and HAp film on the surface of the specimens. According to the pH value and the concentration of Mg^{2+} ions trend depicted in Fig. 8, the ZM31/MgO-CNTs composite demonstrated the lowest pH and Mg^{2+} ion evolution, implying the highest corrosion resistance in accordance with the previous data [63]. It has been observed that the presence of CNTs increases the nucleation sites of hydroxyapatite nuclei, which may decrease and fill the passageways in composite porosities where the SBF solution can enter the composite surface [64].

Fig. 8 indicates the corroded surface morphologies of the sintered specimens of Mg alloy, ZM31/CNTs, and ZM31/MgO-CNTs composites after 7 days of immersion in SBF solution. Corrosion cracks appeared as a result of pitting corrosion in the Mg alloy specimen (Fig. 9a). The Mg alloy formed a thick film of corrosion products, whereas the ZM31/CNTs composite demonstrated thin cracks and smaller corrosion pits and the
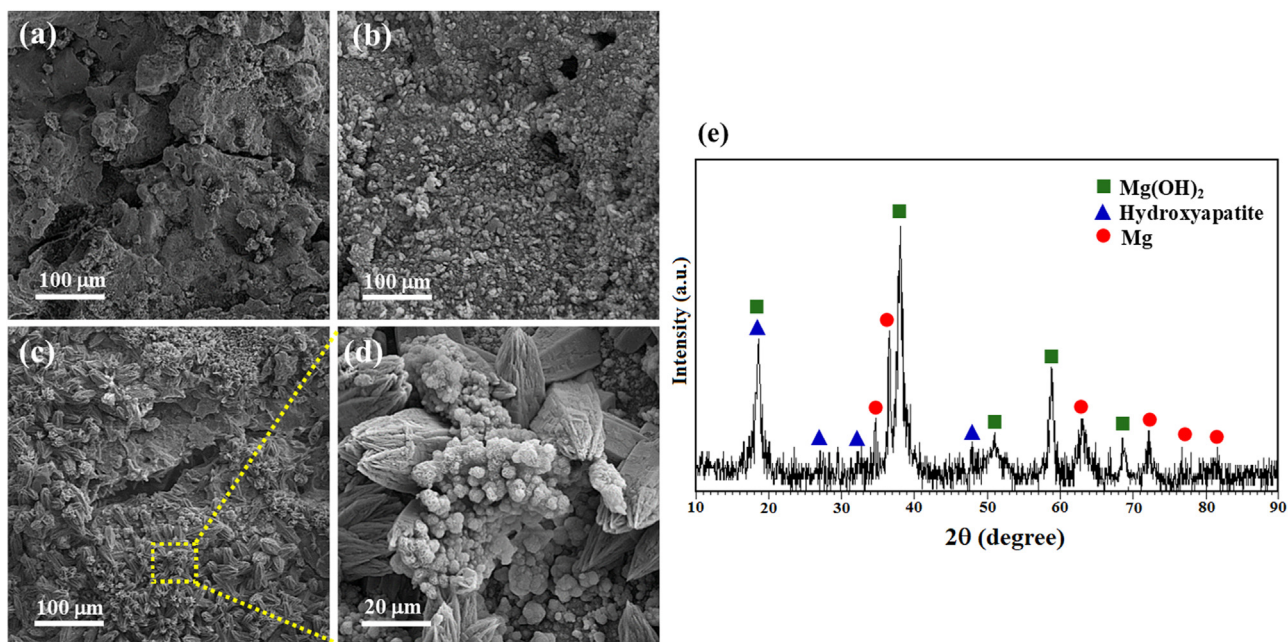
Fig. 8 − SEM photomicrographs of (a) ZM31, (b) ZM31/CNTs, (c,d) ZM31/MgO-CNTs nanocomposites after 7 days of immersion in SBF under physiological condition of 5% CO$_2$ at 37 °C, and (e) XRD pattern of ZM31/MgO-CNTs immersed in SBF for 7 days.
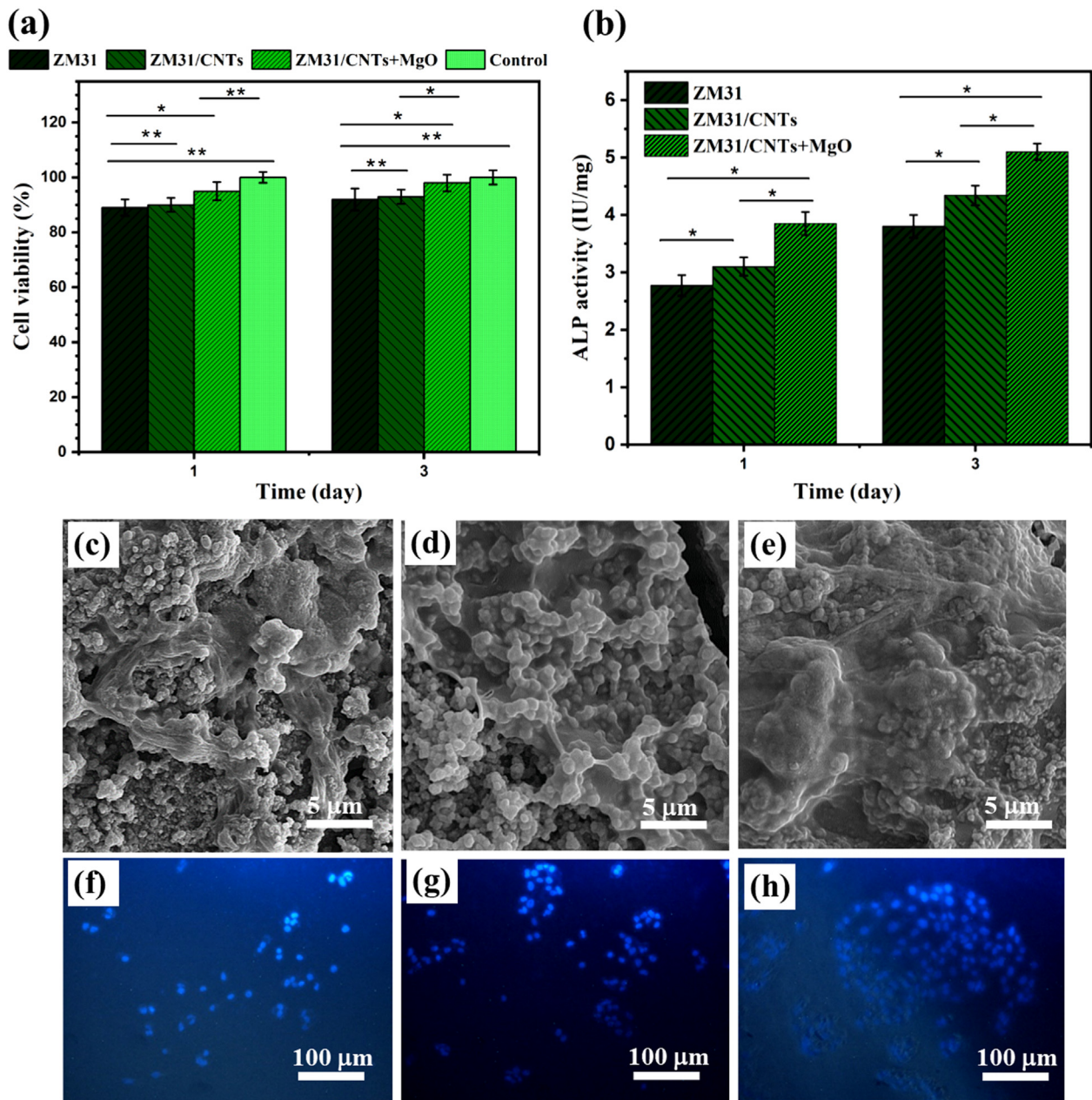
Fig. 9 — (a) Cell viability and (b) ALP activity of MG-63 cells cultured for various times on ZM31 alloys, ZM31/CNTs and MgO-ZM31/CNTs nanocomposites and SEM images of the morphology and adhesion of these MG-6 cells and fluorescent DAPI staining of these cells grown on: (c,f) ZM31 alloy, (d,g) ZM31/CNTs and (e,h) ZM31/MgO-CNTs nanocomposites for 3 days (*p < 0.05 and **p < 0.01).

existence of needle-shaped chlorides (Fig. 9b). These needle-shaped chlorides in the Mg matrix have been proven to break down the corrosion films on the surface, resulting in the creation of deeper corrosion pits [65]. In comparison to the Mg alloy and ZM31/CNTs composite, just a few corrosion pits formed on the ZM31/MgO-CNTs composite, which has a much milder corrosion attack and a more uniform corrosion product film (Fig. 9c) [66]. It is worth mentioning that the presence of HPO_4^{2-} and Ca^{2+} in the SBF causes an accumulation of these ions in the vicinity of the surface, resulting in a supersaturated condition. This situation causes the formation of new HA crystals on the surface of Mg-based composite. Then, as depicted in Fig. 8, needle, cauliflower, and plate-like structures grow and become preferably aligned in the composite surface. Fig. 9e depicts the XRD analysis of the ZM31/MgO-CNTs composite after 7 days of immersion in SBF at 37 °C. XRD analysis of the corroded ZM31/MgO-CNTs composite indicated additional peaks attributed to $Mg(OH)_2$ that were established on the composite surface as just corrosion product, in addition to Mg peaks [66].

3.4. Biocompatibility of the composites

In vitro cell experiments were studied on Mg alloy, ZM31/CNTs, and ZM31/MgO-CNTs composites by using MG-63 cells (Fig. 9). MTT assay was identified in extracts at various times to assess cell viability (Fig. 9a). Cell viability was higher in ZM31/CNTs and ZM31/MgO-CNTs composite extracts than in Mg alloy extracts, and cell activity increased with culture time. The lower cell viability of Mg alloy is associated with a significant number of magnesium ions released from the alloy and an increasing pH value during culture time [48]. Furthermore, during both 1- and 3-day cultivation, the ZM31/MgO-CNTs extract had higher cell viability than the Mg alloy and ZM31/CNTs extracts, which might be attributable to the lower pH and Mg ions concentration in the ZM31/MgO-CNTs composite extract. These findings demonstrated that MgO bounded CNTs surface significantly improved the biocompatibility of Mg-based composites [67]. By adsorbing proteins with special characteristics, CNTs incorporating have been shown to stimulate cell functions; This suggests that CNTs can play a key role in the ability of biomatrix to direct cell growth [68]. It has been claimed that the considerably improved cellular compatibility of ZM31/CNTs composite compared to ZM31 alloy could be attributed to the presence of CNTs, which related to the rough nano-scaled surface topography [68–70].

The MG-63 cells differentiation on ZM31/MgO-CNTs composites was examined using ALP staining (Fig. 9b), as ALP expression has been linked to early cell differentiation. Cells cultured on the ZM31/MgO-CNTs composite showed more intense ALP staining than cells cultured on the Mg alloy, but ZM31/CNTs composites showed less ALP activity than ZM31/MgO-CNTs composites [41]. In this regard, the majority of studies on CNTs-cell interaction found that CNTs had a positive effect on cell behavior. Hahn et al. [71] for example, created CNTs-hydroxyapatite composite samples and tested the answer of pre-osteoblast cells to the samples. They discovered that as the CNT content increased, the proliferation of cells and alkaline phosphate (ALP) activity improved significantly. According to some studies on mesenchymal stem cells (MSCs), it has been shown that CNTs could boost the MSCs differentiation into other chondrocytes and osteoblasts, providing a suitable micro-environment [72]. Furthermore, CNTs were found to be able to move through the cell wall to the nucleus without altering the ultrastructure of the cells [58,73]. These findings showed that the Mg alloy cell response was enhanced using the MgO incorporated CNTs [41].

MG-63 cells were cultured on Mg-based composite for 3 days and then characterized by SEM to assess cell behavior on Mg-based composite in the presence of MgO and CNTs. As shown in Fig. 9c,d,e, representative SEM images were captured to qualitatively evaluate cellular activities, which depict cell morphology. The cells had the typical shape of osteoblasts, indicating that they were growing normally on the surface of the Mg-based composite. At the same culturing time, MG-63 cells cultured on ZM31/MgO-CNTs composites exhibited slightly higher cell attachment than Mg alloy. This was most likely due to faster degradation and alkalinization of the surface, which prevented MG-63 adhesion and possibly caused cell membrane disruption due to oxidative damage.

To qualitatively compare the cellular activities, representative fluorescence images were recorded, as shown in Fig. 9f,g,h, in which the cell nuclei were stained in blue. On Mg alloy, ZM31/CNTs, and ZM31/MgO-CNTs composites, the cells had the typical lens shape of osteoblasts, indicating normal growth behavior. After MgO and CNTs were added to Mg-based composites, the population of MG-63 cells boosted significantly. The improved cell response was attributed to the lower corrosion rate and thus slower ion release and pH enhancement, which was assumed to have a significant effect on the number of cell nuclei on the composite surface [74–82]. These findings show that MgO incorporation to CNT reinforced Mg-based composite can maintain its favorable biocompatibility with osteoblasts in cell attachment and growth.

4. Conclusions

To enhance the mechanical characteristics and corrosion resistance of Mg alloys (ZM31 alloys) for medical implant, biodegradable ZM31/MgO-CNTs composites were designed and prepared using semi-powder metallurgy, followed by hot extrusion. The addition of CNTs and MgO-incorporated CNTs to Mg alloy reduces grain size and increases microhardness by 74.5 and 83.4 HV, respectively. With the addition of CNTs, the UCS of Mg alloy increased to 404.8 MPa, under compressive loading. With MgO-CNTs addition, a maximum UCS of 429 MPa, corresponds to 36% and 44% improvement in UCS of Mg alloy. With the addition of MgO-CNTs fillers, the polarization resistance (R_p) of the ZM31/MgO-CNTs composite increased from 96.48 to 131.61 Ω cm^2. While incorporating CNTs into the Mg alloy matrix results has a less important influence on the corrosion resistance of the Mg-based matrix. Furthermore, the ZM31/MgO-CNTs reinforced Mg-based composite demonstrated good biocompatibility and bioactivity. In this study, the combination of MgO and CNTs provides important concepts for investigating the application potential of MgO-CNTs reinforced Mg-based composites.

Declaration of Competing Interest

The authors declare that they have no known competing financial interests or personal relationships that could have appeared to influence the work reported in this paper.

REFERENCES

[1] Ciobanu G, Harja M. Cerium-doped hydroxyapatite/collagen coatings on titanium for bone implants. Ceram Int 2019;45:2852–7.

[2] Anidha S, Latha N, Muthukkumar M. Reinforcement of Aramid fiber with bagasse epoxy bio-degradable composite: investigations on mechanical properties and surface morphology. J Mater Res Technol 2019;8:3198–212.

[3] Meng F, Du W, Lou F, Du X, Zhao C, Liu K, et al. Dispersion of CNT via an effective two-step method, and enhanced

thermal conductivity of Mg composite reinforced by the dispersed CNT. Mater Chem Phys 2022;278:125683.

[4] Moghadasi K, Mohd Isa MS, Ariffin MA, Mohd jamil MZ, Raja S, Wu B, et al. A review on biomedical implant materials and the effect of friction stir based techniques on their mechanical and tribological properties. J Mater Res Technol 2022;17:1054—121.

[5] Heise S, Wirth T, Höhlinger M, Hernández YT, Ortiz JAR, Wagener V, et al. Electrophoretic deposition of chitosan/bioactive glass/silica coatings on stainless steel and WE43 Mg alloy substrates. Surf Coating Technol 2018;344:553—63.

[6] Abazari S, Shamsipur A, Bakhsheshi-Rad HR, Ismail AF, Sharif S, Razzaghi M, et al. Carbon nanotubes (CNTs)-reinforced magnesium-based matrix composites: a comprehensive review. Materials 2020;13(19):4421.

[7] Yu W, Sun R, Guo Z, Wang Z, He Y, Lu G, et al. Novel fluoridated hydroxyapatite/MAO composite coating on AZ31B magnesium alloy for biomedical application. Appl Surf Sci 2019;464:708—15.

[8] Tabasum S, Noreen A, Kanwal A, Zuber M, Anjum MN, Zia KM. Glycoproteins functionalized natural and synthetic polymers for prospective biomedical applications: a review. Int J Biol Macromol 2017;98:748—76.

[9] Santerre JP, Woodhouse K, Laroche G, Labow RS. Understanding the biodegradation of polyurethanes: from classical implants to tissue engineering materials. Biomaterials 2005;26:7457—70.

[10] Khazeni D, Saremi M, Soltani R. Development of HA-CNTs composite coating on AZ31 magnesium alloy by cathodic electrodeposition. Part 1: microstructural and mechanical characterization. Ceram Int 2019;45:11174—85.

[11] Witte F, Fischer J, Nellesen J, Crostack H-A, Kaese V, Pisch A, et al. In vitro and in vivo corrosion measurements of magnesium alloys. Biomaterials 2006;27:1013—8.

[12] Du P, Li K, Zhu B, Xiang T, Xie G. Development of non-toxic low-cost bioactive porous Ti—Fe—Si bulk metallic glass with bone-like mechanical properties for orthopedic implants. J Mater Res Technol 2022;17:1319—29.

[13] Zhang E, Yin D, Xu L, Yang L, Yang K. Microstructure, mechanical and corrosion properties and biocompatibility of Mg—Zn—Mn alloys for biomedical application. Mater Sci Eng C 2009;29:987—93.

[14] Babu MM, Rao PV, Singh RK, Kim H-W, Veeraiah N, Özcan M, et al. ZnO incorporated high phosphate bioactive glasses for guided bone regeneration implants: enhancement of in vitro bioactivity and antibacterial activity. J Mater Res Technol 2021;15:633—46.

[15] Wang X, Dong LH, Ma XL, Zheng YF. Microstructure, mechanical property and corrosion behaviors of interpenetrating C/Mg-Zn-Mn composite fabricated by suction casting. Mater Sci Eng C 2013;33:618—25.

[16] Abazari S, Shamsipur A, Bakhsheshi-Rad HR, Ramakrishna S, Berto F. Graphene family nanomaterial reinforced magnesium-based matrix composites for biomedical application: a comprehensive review. Metals 2020;10(8):1002.

[17] Bornapour M, Muja N, Shum-Tim D, Cerruti M, Pekguleryuz M. Biocompatibility and biodegradability of Mg—Sr alloys: the formation of Sr-substituted hydroxyapatite. Acta Biomater 2013;9:5319—30.

[18] Yang L, Shi X, Tian X, Xue Y, Wang J, Qi L. Influence of pH value on the microstructure and corrosion behavior of carbon fiber reinforced magnesium matrix composites. J Mater Res Technol 2022;17:412—24.

[19] Saberi A, Bakhsheshi-Rad HR, Abazari S, Ismail AF, Sharif S, Ramakrishna S, et al. A comprehensive review on surface modifications of biodegradable magnesium-based implant alloy: polymer coatings opportunities and challenges. Coatings 2021;11(7):747.

[20] Lu Y, Bradshaw AR, Chiu YL, Jones IP. Effects of secondary phase and grain size on the corrosion of biodegradable Mg—Zn—Ca alloys. Mater Sci Eng C 2015;48:480—6.

[21] Yin D, Zhang E, Zeng S. Effect of Zn on mechanical property and corrosion property of extruded Mg-Zn-Mn alloy. Trans Nonferrous Met Soc China 2008;18:763—8.

[22] Xu L, Zhang E, Yin D, Zeng S, Yang K. In vitro corrosion behaviour of Mg alloys in a phosphate buffered solution for bone implant application. J Mater Sci Mater Med 2008;19:1017—25.

[23] Morisada Y, Fujii H, Nagaoka T, Fukusumi M. MWCNTs/AZ31 surface composites fabricated by friction stir processing. Mater Sci Eng, A 2006;419:344—8.

[24] Goh CS, Wei J, Lee LC, Gupta M. Simultaneous enhancement in strength and ductility by reinforcing magnesium with carbon nanotubes. Mater Sci Eng, A 2006;423:153—6.

[25] Goh CS, Wei J, Lee LC, Gupta M. Development of novel carbon nanotube reinforced magnesium nanocomposites using the powder metallurgy technique. Nanotechnology 2005;17:7.

[26] Qian M, Goh CS, Sun YH, Ng FL. Effects of CNTs on microstructure and hardness of laser welds of the CNT-reinforced magnesium composite. Compos Part A Appl Sci Manuf 2013;48:67—72.

[27] Wong KKH, Zinke-Allmang M, Hutter JL, Hrapovic S, Luong JHT, Wan W. The effect of carbon nanotube aspect ratio and loading on the elastic modulus of electrospun poly (vinyl alcohol)-carbon nanotube hybrid fibers. Carbon N Y 2009;47:2571—8.

[28] Chen X, Xia J, Peng J, Li W, Xie S. Carbon-nanotube metal-matrix composites prepared by electroless plating. Compos Sci Technol 2000;60:301—6.

[29] Paramsothy M, Chan J, Kwok R, Gupta M. Addition of CNTs to enhance tensile/compressive response of magnesium alloy ZK60A. Compos Part A Appl Sci Manuf 2011;42:180—8.

[30] Coleman JN, Curran S, Dalton AB, Davey AP, McCarthy B, Blau W, et al. Percolation-dominated conductivity in a conjugated-polymer-carbon-nanotube composite. Phys Rev B 1998;58:R7492.

[31] Huang Y, Li J, Wan L, Meng X, Xie Y. Strengthening and toughening mechanisms of CNTs/Mg-6Zn composites via friction stir processing. Mater Sci Eng, A 2018;732:205—11.

[32] Sun F, Shi C, Rhee KY, Zhao N. In situ synthesis of CNTs in Mg powder at low temperature for fabricating reinforced Mg composites. J Alloys Compd 2013;551:496—501.

[33] Rashad M, Pan F, Asif M, Li L. Enhanced ductility of Mg—3Al—1Zn alloy reinforced with short length multi-walled carbon nanotubes using a powder metallurgy method. Prog Nat Sci Mater Int 2015;25:276—81.

[34] Endo M, Hayashi T, Itoh I, Kim YA, Shimamoto D, Muramatsu H, et al. An anticorrosive magnesium/carbon nanotube composite. Appl Phys Lett 2008;92:63105.

[35] Kondoh K, Fukuda H, Umeda J, Imai H, Fugetsu B, Endo M. Microstructural and mechanical analysis of carbon nanotube reinforced magnesium alloy powder composites. Mater Sci Eng, A 2010;527:4103—8.

[36] Yuan Q, Zeng X, Liu Y, Luo L, Wu J, Wang Y, et al. Microstructure and mechanical properties of AZ91 alloy reinforced by carbon nanotubes coated with MgO. Carbon 2016;96:843—55.

[37] Du YZ, Qiao XG, Zheng M-Y, Wang DB, Wu K, Golovin IS. Effect of microalloying with Ca on the microstructure and mechanical properties of Mg-6 mass% Zn alloys. Mater Des 2016;98:285—93.

[38] Standard test methods of compression testing of metallic materials at room temperature. ASTM international; 2009. https://doi.org/10.1520/E0009-09.

[39] American Society for Testing and Materials (Filadelfia P. Astm G31-72: standard practice for laboratory immersion corrosion testing of metals. ASTM; 2004.

[40] Saberi A, Bakhsheshi-Rad HR, Karamian E, Kasiri-Asgarani M, Ghomi H. Magnesium-graphene nano-platelet composites: corrosion behavior, mechanical and biological properties. J Alloys Compd 2020 Apr 25;821:153379.

[41] Shuai C, Wang B, Bin S, Peng S, Gao C. Interfacial strengthening by reduced graphene oxide coated with MgO in biodegradable Mg composites. Mater Des 2020:108612.

[42] Hou J, Du W, Parande G, Gupta M, Li S. Significantly enhancing the strength + ductility combination of Mg-9Al alloy using multi-walled carbon nanotubes. J Alloys Compd 2019;790:974—82.

[43] Karthika V, Kaleeswarran P, Gopinath K, Arumugam A, Govindarajan M, Alharbi NS, et al. Biocompatible properties of nano-drug carriers using TiO2-Au embedded on multiwall carbon nanotubes for targeted drug delivery. Mater Sci Eng C 2018;90:589—601.

[44] Nai MH, Wei J, Gupta M. Interface tailoring to enhance mechanical properties of carbon nanotube reinforced magnesium composites. Mater Des 2014;60:490—5.

[45] Hull D, Bacon DJ. Introduction to dislocations. Butterworth-Heinemann; 2001.

[46] Yuan Q, Zhou G, Liao L, Liu Y, Luo L. Interfacial structure in AZ91 alloy composites reinforced by graphene nanosheets. Carbon N Y 2018;127:177—86.

[47] Rashad M, Pan F, Tang A, Asif M, Aamir M. Synergetic effect of graphene nanoplatelets (GNPs) and multi-walled carbon nanotube (MW-CNTs) on mechanical properties of pure magnesium. J Alloys Compd 2014;603:111—8.

[48] Zhang J, Wen Z, Zhao M, Li G, Dai C. Effect of the addition CNTs on performance of CaP/chitosan/coating deposited on magnesium alloy by electrophoretic deposition. Mater Sci Eng C 2016;58:992—1000.

[49] Lei T, Ouyang C, Tang W, Li L-F, Zhou L-S. Enhanced corrosion protection of MgO coatings on magnesium alloy deposited by an anodic electrodeposition process. Corros Sci 2010;52:3504—8.

[50] Parizi MT, Ebrahimi GR, Ezatpour HR, Paidar M. The structure effect of carbonaceous reinforcement on the microstructural characterization and mechanical behavior of AZ80 magnesium alloy. J Alloys Compd 2019;809:151682.

[51] Pei X, Wang J, Wan Q, Kang L, Xiao M, Bao H. Functionally graded carbon nanotubes/hydroxyapatite composite coating by laser cladding. Surf Coating Technol 2011;205:4380—7.

[52] Tsui YC, Doyle C, Clyne TW. Plasma sprayed hydroxyapatite coatings on titanium substrates Part 1: mechanical properties and residual stress levels. Biomaterials 1998;19:2015—29.

[53] Yu L-G, Khor KA, Li H, Cheang P. Effect of spark plasma sintering on the microstructure and in vitro behavior of plasma sprayed HA coatings. Biomaterials 2003;24:2695—705.

[54] Khabazian S, Sanjabi S. The effect of multi-walled carbon nanotube pretreatments on the electrodeposition of Ni—MWCNTs coatings. Appl Surf Sci 2011;257:5850—6.

[55] Daneshvar-Fatah F, Nasirpouri F. A study on electrodeposition of Ni-noncovalently treated carbon nanotubes nanocomposite coatings with desirable mechanical and anti-corrosion properties. Surf Coating Technol 2014;248:63—73.

[56] Li H, Song X, Li B, Kang J, Liang C, Wang H, et al. Carbon nanotube-reinforced mesoporous hydroxyapatite composites with excellent mechanical and biological properties for bone replacement material application. Mater Sci Eng C 2017;77:1078—87.

[57] Lei T, Wang L, Ouyang C, Li N, Zhou L. In situ preparation and enhanced mechanical properties of carbon nanotube/hydroxyapatite composites. Int J Appl Ceram Technol 2011;8:532—9.

[58] Gao C, Feng P, Peng S, Shuai C. Carbon nanotube, graphene and boron nitride nanotube reinforced bioactive ceramics for bone repair. Acta Biomater 2017;61:1—20.

[59] Han J, Luthringer B, Tang S, Hu J, Blawert C, Zheludkevich ML. Evolution and performance of a MgO/HA/DCPD gradient coating on pure magnesium. J Alloys Compd 2021;883:160793.

[60] Dutta S, Gupta S, Roy M. Recent developments in magnesium metal—matrix composites for biomedical applications: a review. ACS Biomater Sci Eng 2020;6:4748—73.

[61] Khalajabadi SZ, Kadir MR, Izman S, Bakhsheshi-Rad HR, Farahany S. Effect of mechanical alloying on the phase evolution, microstructure and bio-corrosion properties of a Mg/HA/TiO2/MgO nanocomposite. Ceram Int 2014;40(10):16743—59.

[62] Cai S, Lei T, Li N, Feng F. Effects of Zn on microstructure, mechanical properties and corrosion behavior of Mg—Zn alloys. Mater Sci Eng C 2012;32:2570—7.

[63] Lin G, Liu D, Chen M, You C, Li Z, Wang Y, et al. Preparation and characterization of biodegradable Mg-Zn-Ca/MgO nanocomposites for biomedical applications. Mater Charact 2018;144:120—30.

[64] Khazeni D, Saremi M, Soltani R. Development of HA-CNTs composite coating on AZ31 Magnesium alloy by cathodic electrodeposition. Part 2: electrochemical and in-vitro behavior. Ceram Int 2019;45:11186—94.

[65] Zeng R-C, Li X-T, Li S-Q, Zhang F, Han E-H. In vitro degradation of pure Mg in response to glucose. Sci Rep 2015;5:1—14.

[66] Shahin M, Munir K, Wen C, Li Y. Magnesium-based composites reinforced with graphene nanoplatelets as biodegradable implant materials. J Alloys Compd 2020;828:154461.

[67] Shuai C, Wang B, Bin S, Peng S, Gao C. TiO2-Induced in situ reaction in graphene oxide-reinforced AZ61 biocomposites to enhance the interfacial bonding. ACS Appl Mater Interfaces 2020;12:23464—73.

[68] Li X, Liu X, Huang J, Fan Y, Cui F. Biomedical investigation of CNT based coatings. Surf Coating Technol 2011;206:759—66.

[69] Pan L, Pei X, He R, Wan Q, Wang J. Multiwall carbon nanotubes/polycaprolactone composites for bone tissue engineering application. Colloids Surf B Biointerfaces 2012;93:226—34.

[70] Li X, Gao H, Uo M, Sato Y, Akasaka T, Feng Q, et al. Effect of carbon nanotubes on cellular functions in vitro. J Biomed Mater Res Part A An Off J Soc Biomater Japanese Soc Biomater Aust Soc Biomater Korean Soc Biomater 2009;91:132—9.

[71] Hahn B-D, Lee J-M, Park D-S, Choi J-J, Ryu J, Yoon W-H, et al. Mechanical and in vitro biological performances of hydroxyapatite—carbon nanotube composite coatings deposited on Ti by aerosol deposition. Acta Biomater 2009;5:3205—14.

[72] Namgung S, Baik KY, Park J, Hong S. Controlling the growth and differentiation of human mesenchymal stem cells by the arrangement of individual carbon nanotubes. ACS Nano 2011;5:7383—90.

[73] Mooney E, Dockery P, Greiser U, Murphy M, Barron V. Carbon nanotubes and mesenchymal stem cells: biocompatibility, proliferation and differentiation. Nano Lett 2008;8:2137—43.

[74] Mao L, Zhu H, Chen L, Zhou H, Yuan G, Song C. Enhancement of corrosion resistance and biocompatibility of Mg-Nd-Zn-Zr alloy achieved with phosphate coating for vascular stent application. J Mater Res Technol 2020;9:6409—19.

[75] Rajan S, Marimuthu K, Ayyanar CB, Khan A, Siengchin S, Rangappa SM. In-vitro cytotoxicity of zinc oxide, graphene oxide, and calcium carbonate nano particulates reinforced

high-density polyethylene composite. J Mater Res Technol 2022;18:921—30.

[76] Xu JL, Tang J, Hu J, Zhang JL, Luo JM, Hao GD, et al. Microstructure, degradation properties and cytocompatibility of micro-arc oxidation coatings on the microwave sintered Ti-15Mg metal-metal composite. J Mater Res Technol 2021;11:1654—64.

[77] Yu L, Lyu S, Chen Y, You C, Zhao Y, Chen M. Simultaneously improving the mechanical property and corrosion resistance of extruded biomedical Mg—3Zn alloy by forming in-situ MgO. J Mater Res Technol 2022;18:2977—92.

[78] Hu H, Wang X, Huang Y, Yang Z, Jia B, Sun K, et al. Electrochemical techniques for monitoring the biodegradability of nanocomposite Mg-alloy/HA for repairing bone fracture. J Mater Res Technol 2022;18:1669—81.

[79] Guo Y, Xu Z, Liu M, Zu S, Yang Y, Wang Q, et al. The corrosion resistance, biocompatibility and biomineralization of the dicalcium phosphate dihydrate coating on the surface of the additively manufactured NiTi alloy. J Mater Res Technol 2022;17:622—35.

[80] Khorashadizade F, Abazari S, Rajabi M, Bakhsheshi-Rad HR, Ismail AF, Sharif S, et al. Overview of magnesium-ceramic composites: mechanical, corrosion and biological properties. J Mater Res Technol 2021;15:6034—66.

[81] Naalchian M, Kasiri-Asgarani M, Shamanian M, Bakhtiari R, Bakhsheshi-Rad HR. Effect of substrate's heat treatment on microstructure and mechanical properties TLP bonding of dissimilar X-45/FSX-414 cobalt based superalloys. Met Mater Int 2021;27(11):4657—68.

[82] Abazari S, Shamsipur A, Bakhsheshi-Rad HR. Reduced graphene oxide (RGO) reinforced Mg biocomposites for use as orthopedic applications: Mechanical properties, cytocompatibility and antibacterial activity. J Magnes Alloy 2021.